The Vorticity Balance of the Ocean Surface in Hawaii from a Regional Reanalysis*

JOAO MARCOS AZEVEDO CORREIA DE SOUZA, BRIAN POWELL, ALMA CAROLINA CASTILLO-TRUJILLO, AND PIERRE FLAMENT

Department of Oceanography, School of Ocean and Earth Science and Technology, University of Hawai'i at Mānoa, Honolulu, Hawaii

(Manuscript received 21 April 2014, in final form 20 October 2014)

ABSTRACT

The ocean surface vorticity budget around the Hawaiian Islands is examined using an 18-month model reanalysis generated using four-dimensional variational state estimation with all available observations (satellite, in situ, and high-frequency radio). To better resolve the ocean surface currents and reduce the representation error of the radio-measured surface currents, this study developed a new vertical scheme for the Regional Ocean Modeling System. A new, detailed description of the ocean surface vorticity is created, revealing a region dominated by cyclonic (anticyclonic) vorticity to the north (south) of the mean position of the Hawaii Lee Countercurrent. Advection of vorticity is the primary process that transports the vorticity generated in the lee of the islands by the wind wake. In this island lee, the zonal wavenumber spectra show a cascade of vorticity/energy from the submesoscale toward the larger scales. Latitudinal differences in the advection of vorticity spectra indicate the propagation of a first baroclinic mode Rossby wave in the region dominated by anticyclonic vorticity to the west of the island of Hawaii, while the region dominated by cyclonic vorticity is disrupted by the wake of the smaller islands.

1. Introduction

The Hawaiian Island chain has a significant influence on the oceanic and atmospheric circulation of the western subtropical Pacific (e.g., Xie et al. 2001; Chavanne et al. 2002). The islands disrupt the subtropical gyre circulation resulting in a complex wake because of the blocking of the westward-flowing North Equatorial Current (NEC). In the atmosphere, the island mountains penetrate the inversion layer, disrupting the northeasterly trade winds, resulting in dipolelike structures in the wind stress curl that act on the ocean surface generating Ekman pumping velocities of approximately $3\,\mathrm{m\,day^{-1}}$ (Chavanne et al. 2002; Qu et al. 2008). These atmospheric and oceanic wake effects generate complex oceanic dynamics in the Hawaiian Archipelago, including strong eddies generated in the lee of the islands. Using surface drifter trajectories, Lumpkin (1998) identified the canonical circulation around Hawaii (as shown in Fig. 1a): the NEC impacts the archipelago around the island of Hawaii, as this flow bifurcates with the NEC flowing west around the southern end of the island and a second flow to the north of the archipelago referred to as the North Hawaiian Ridge Current (NHRC). The strong wake in the winds (Xie et al. 2001) generates a countercurrent, the Hawaiian Lee Countercurrent (HLCC), that impacts the leeward side of the island of Hawaii and is redirected to the north following the southern side of the archipelago creating the Hawaii Lee Current (HLC).

Lumpkin and Flament (2001) mapped the ocean surface vorticity and found a pattern in the lee of the islands of cyclonic vorticity to the north and anticyclonic vorticity to the south of 19.5°N, the approximate latitude of the HLCC (see Fig. 1 of Lumpkin and Flament 2001). Because of the scarcity of the available drifter data, they could not describe the surface ocean vorticity and its balance. Revisiting this region, Lumpkin and Flament (2013) studied the energetics of the ocean currents using a more extensive dataset of 15-m depth drogue drifters that provided more detailed data of the mean circulation and the eddy kinetic energy; however, this dataset is still not able to describe the vorticity balance of the ocean surface.

* School of Ocean and Earth Science and Technology Publication Number 9170.

Corresponding author address: Joao Marcos Azevedo Correia de Souza, Department of Oceanography, University of Hawai'i at Mānoa, 1000 Pope Rd., MSB, Honolulu, 96822 HI.
E-mail: jsouza@soest.hawaii.edu

DOI: 10.1175/JPO-D-14-0074.1

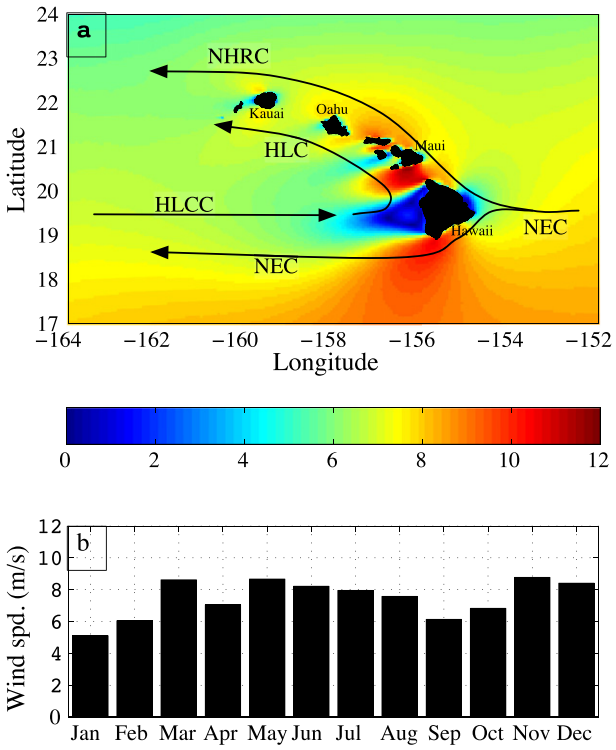

FIG. 1. (a) Schematic map of the mean currents in Hawaii overlaid on the mean wind intensity ($m\,s^{-1}$) from the WRF Model. (b) Monthly averaged histogram of wind speed for the channel between the islands of Hawaii and Maui.

Other impacts on the ocean surface vorticity are related to the wind forcing away from the island wake region. Xie et al. (2001) analyzed how the ocean, by adjusting its SST, provides a feedback mechanism for the wake extension to the west. They observed wind anomalies as far west as 175°E (over 3000 km from the island), 10 times longer than any island wake observed previously. Moreover, Sasaki et al. (2013) showed how ocean–atmosphere coupled processes over the HLCC are responsible for the amplification of its seasonal and interannual variability. Understanding the ocean surface vorticity balance may explain how the currents originally driven by an orographic wind wake can evolve into a coupled ocean–atmosphere disturbance that is capable of driving an eastward flow like the HLCC and help identify the processes relevant to this transition.

In addition to the coupled processes, baroclinic tides play an important role in the transfer of energy into the ocean interior as well as circulation around the islands. The Hawaiian Archipelago is a significant site of barotropic tidal dissipation with estimates of up to 20 GW from M_2 alone. This is due to the ridges of the archipelago situated orthogonally to the propagation of the M_2 that results in significant semidiurnal baroclinic tides radiating from the ridges (Dushaw et al. 1995; Ray and Mitchum 1996, 1997). Carter et al. (2008) used a numerical model to determine an energy budget of the tides around Kaena Ridge off the northwest coast of the island of Oahu. They found that 2.7 GW of energy is dissipated from the barotropic tide along the ridge with 2.3 GW of that energy converted directly into baroclinic tides. The local generation over the ridge is highly variable and is sensitive to both local stratification changes (due to eddies, etc.) as well as advection of baroclinic tidal energy from remote generation sites (Zilberman et al. 2011; Powell et al. 2012).

High-resolution numerical simulations are important tools for understanding ocean processes where data coverage is scarce. Ocean general circulation models (OGCMs) have been developed to resolve the diversity of oceanic processes and scales ranging from the global to regional. A difference between existing OGCMs is the vertical discretization system used. It affects the way a model represents the ocean properties and resolves important processes, such as boundary currents, baroclinic waves, and mixing. Terrain-following models are largely used for regional simulations, and the Regional Ocean Modeling System (ROMS) has been particularly popular in the oceanographic community in the last decade.

Taking advantage of the increasing number of available oceanic data, four-dimensional variational data assimilation (4D-Var) state estimation techniques are used to constrain the model solutions to the observations, yielding estimates of the ocean circulation that are more reliable than either alone (Powell et al. 2008). This approach can provide an accurate reanalysis of the regional circulation. Daily information about the global sea surface temperature (SST) is available from a combination of different satellite sensors. While the SSTs are usually calibrated to represent the near-surface of the ocean, the thickness of the model first layer may vary between 50 cm and 10 m. This issue is particularly important for the assimilation of SST into numerical models and when trying to represent the diurnal variability of SST in the simulations.

Coastal high-frequency radio (HFR) currents provide an increasing amount of high-resolution surface current data. These data are a unique source for validation of model forecasts and data assimilation efforts. While early works focused on the assimilation of the low-frequency circulation obtained from the HFR, in which the higher-frequency inertial and tidal signals are removed from the dataset prior to the assimilation (e.g., Lewis et al. 1998), recent efforts aimed at the assimilation of the full circulation (e.g., Shulman and Paduan 2009).

The objective of the present work is to examine the surface ocean dynamics around the Hawaiian Archipelago

to quantify the contribution from regional ocean processes and the atmosphere to the ocean surface vorticity budget. To quantify the vorticity budget, we generate a 4D-Var data assimilation reanalysis using the ROMS for the Hawaiian Islands region based on the work of Matthews et al. (2012). Special consideration was made to accurately represent the ocean surface, including 1) a modification of the vertical coordinate system used in ROMS and 2) an analysis of how to represent the HFR radial velocities for the model in a region with strong baroclinic tidal flow. The focus is primarily on the surface currents. The domain covers the main Hawaiian Islands (Fig. 1a) with a complex bathymetry, including perturbations generated by the wake of the islands, their westward propagation, and impacts on the mean flow pattern.

2. Methods

a. Model

ROMS is a 3D primitive equation ocean model, with potential temperature, salinity, and a nonlinear equation of state, using hydrostatic and Boussinesq approximations. A full description of the model can be found in Shchepetkin and McWilliams (2005, 2009) and on the ROMS website (www.myroms.org). In this paper, we focus on the discussion of the terrain-following coordinate system.

The present model configuration is equivalent to the one used by Matthews et al. (2012), except for modifications to the vertical coordinate and assimilated datasets used. The domain corresponds to the main Hawaiian Archipelago with 4-km horizontal resolution and 32 vertical layers. The model uses initial and boundary conditions provided by the global Hybrid Coordinate Ocean Model (HYCOM) (Bleck 2002) using the Navy Coupled Ocean Data Assimilation (NCODA) as described by Cummings (2005). The surface forcing fields are prescribed from a locally produced Weather Research and Forecasting (WRF) Model generated operationally as part of the Pacific Islands Integrated Ocean Observing System (PacIOOS) project (Tu and Chen 2011). As shown in Fig. 1a, the WRF Model well represents the blocking of the trade winds by the islands, creating areas of weak winds in the western lee of the islands and an intensification of the winds through the island channels. The resulting wind stress curl compares very well to that observed by Chavanne et al. (2002) using scatterometer data and is discussed in section 4. Hawaii is dominated by the northeasterly trade winds year-round with episodes of weakened or inverted winds with the passage of frontal systems in the atmosphere. A seasonal cycle in the monthly averaged wind intensity is found in the WRF Model during the period that varies approximately between 5 and 10 $\mathrm{m\,s^{-1}}$ (Fig. 1b) and compares well with climatology.

Because the tidal flow is such a significant portion of the circulation of the region, 11 constituents obtained from the Oregon State University TOPEX/Poseidon Global Inverse Solution (TPXO) (Egbert and Erofeeva 2002) were introduced as a separate spectral forcing at the boundaries to the free surface and barotropic velocity.

b. Vertical coordinate system

ROMS uses a generalization of the classic terrain-following vertical coordinate system (σ coordinates), defined as s coordinates. It divides the water column in a series of σ layers, a nondimensional coordinate varying between 0 at the ocean surface and -1 at the ocean bottom. Stretching functions are used to improve the resolution near the surface and bottom boundaries. ROMS provides four stretching functions as part of the code. In addition, a transformation function is required to map from the σ coordinates to the layer depth depending upon the water depth and free-surface elevation.

In the standard ROMS configuration, σ is defined as a linear function, discretized in constant intervals proportional to the number of layers used in the simulation. Because layer depths are proportional to both the free-surface height and the water depth, their thicknesses vary in both space and time. While the free surface has a small amplitude in comparison to the layer thicknesses, the same cannot be said about water depth. In regions of large depth variation, such as the Hawaiian Islands (where depths vary from 10 to 6000 m), a relatively large variation in the layer thicknesses is expected. One way to minimize this is to increase the number of vertical layers; however, the increase in computational cost may be impracticable, particularly for state estimation experiments.

ROMS does not have a specific equation to solve the SST or sea surface salinity (SSS). These properties are represented by the surface model layer, with thickness between $\approx$0.6 and 4.2 m for the present grid using the VS4 (see the appendix). This is problematic for representing the SST diurnal variability since thicker layers respond slower to momentum and heat flux variations. Constraining the spatial variation of the surface layer thickness is important to improve our representation of ocean surface properties around Hawaii. To accomplish this, we developed a new stretching function to give a constraint to the ocean surface layer. This new scheme is developed (dubbed VS5) in the appendix with detailed results. Overall, the new scheme results in a surface layer thickness no greater than 2.5 m for our

domain, with many surface layer cells being less than 1 m thick. This improves our representation of the ocean–atmosphere boundary where changes in both the heat and momentum flux can be quite short and are underrepresented when the surface layer is represented by a larger mass of water.

3. Hawaii reanalysis

Using the VS5 scheme for the vertical coordinate (see the appendix), three experiments with 4D-Var state estimation were performed to generate a reanalysis for the Hawaiian Archipelago. The same 4D-Var configuration detailed by Matthews et al. (2012) was used. Daily SST fields from the Moderate Resolution Infrared Spectroradiometer (MODIS) satellite, along-track SSH from the *Jason-2* platforms in the form of sea level anomalies (SLA), synthetic SLA obtained from the global HYCOM–NCODA simulation, and temperature and salinity from both ocean gliders and Argo profiling floats were assimilated in all the experiments. The experiments differ by the assimilation of the following:

Experiment A, all data with unfiltered (raw) HFR radial surface velocities.
Experiment B, all data with low-pass filtered HFR radial surface velocities.
Experiment C, all data, but withhold all HFR radial surface velocities.

Each experiment was initially integrated for 1 month for comparison purposes. The setup with best performance (experiment A) was integrated for 18 months, from January 2011 to July 2012, combining the model and data via 4D-Var to generate an oceanic reanalysis used for the study of the vorticity balance.

a. Datasets

The datasets assimilated in the model and used for validation of the simulation results are ocean SeaGlider temperature and salinity, Argo profiling float temperature and salinity, MODIS SST, *Jason-2* along-track SSH, HFR radial velocities (except for experiment C), and synthetic SLA fields from the global HYCOM simulation.

SeaGliders are buoyancy-driven vehicles that can be remotely controlled to follow predetermined paths and sampling strategies (Eriksen et al. 2001). Argo is a global ocean observing system for the twenty-first century composed of approximately 3000 profiling floats measuring temperature and salinity down to 2000-m depth, every 10 days (Oka and Ando 2004). The MODIS level-2 SST data are available from the Physical Oceanography Distributed Active Archive Center (PO.DAAC), NASA. For this region, the lee of the islands yields a higher number of SST observations because of the smaller cloud coverage.

For SSH, along-track SLA from the *Jason-2* satellite is available roughly every 3 days in the region covered by the model grid. The mean SSH from a 6-yr climatology of our model is added to the observations to provide a consistent dynamic mean.

The ROMS boundary conditions are provided by the $^1/_{12}^\circ$ resolution global HYCOM–NCODA simulation that is assimilating the global SSH. The HYCOM–NCODA product uses a multivariate optimal interpolation scheme to assimilate available satellite altimeter observations, satellite and in situ SST, as well as available in situ vertical temperature and salinity profiles from XBTs, ARGO floats, and moored buoys (Cummings 2005). For these experiments, we also utilize generated synthetic SLA obtained from the HYCOM–NCODA by removing the mean HYCOM–NCODA SSH field and replacing it with the mean ROMS field. The along-track *Jason-2* dataset provides approximately two to three passes per week across our model domain, while the HYCOM simulation provides daily information for the entire domain. The representation errors for these synthetic observations were calculated based on the HYCOM–NCODA SLA standard deviation and are over 2 times the error used for the along-track data.

For the purposes of the present study, the primary dataset examined is the HFR radial velocities obtained south of Oahu. The HFR radial velocities were sampled at an antenna located at Kalaeloa (21.3°N, 158.1°W). A 60-km range limit was used to minimize the contamination from noise present at the edge of the coverage area. Two approaches were used to process the data prior to its assimilation in the model:

(i) Raw—The HFR data were averaged every 2 h to remove sampling errors and high-frequency variability that is not represented by the model.
(ii) Low pass—The baroclinic tides around the island are a dominant forcing in the surface currents (Carter et al. 2008); however, the surfacing of these internal tides is a red spectrum, random process because of the variability in the baroclinic tide conversion propagation through changing stratification (Chavanne et al. 2010; Powell et al. 2012; Kerry et al. 2014). There are at least four significant reasons that the model will have a different realization of the surface tidal currents: the model is discretized, the slope of the barotropic-to-baroclinic tide conversion ridge is slightly different, stratification will not be perfectly identical to reality, and numerical dissipation and mixing will not perfectly match the mixing present in the baroclinic tide. As such, the model may have

TABLE 1. Comparison between the data assimilation experiments and the data. The columns represent the basic statistics of the differences between the observed satellite SLA (*Jason-2* and *Envisat*), SST (MODIS), and HFR radial velocities and the simulation results.

	SLA (m)			SST (°C)			Low frequency radial velocity ($cm\,s^{-1}$)		
	RMSD ± std	Max diff	Min diff	RMSD ± std	Max diff	Min diff	RMSD ± std	Max diff	Min diff
Experiment A	0.05 ± 0.06	0.25	−0.26	0.25 ± 0.25	1.16	−3.84	6.5 ± 6	42	−35
Experiment B	0.05 ± 0.05	0.24	−0.24	0.26 ± 0.25	1.07	−3.67	8.8 ± 8	58	−58
Experiment C	0.06 ± 0.06	0.30	−0.23	0.28 ± 0.26	0.95	−3.83	14.9 ± 14	69	−72

a slightly different phasing and location of baroclinic tidal currents as observed by the radar. It is expected that the model behaves well and minimizes these errors, but they may be significant (Janeković and Powell 2012). In addition, the (somewhat) random phase and location of the surfacing baroclinic tide prevents us from filtering at specific spectral frequencies. To account for these differences, a second set of HFR data is examined. Before assimilation, a 48-h low-pass Butterworth filter was applied to the HFR radials to remove the tidal and inertial frequencies from the data. The ROMS prediction was then high-pass filtered at 48 h to generate a prediction of what the high-frequency signal, including the contribution by the barotropic and baroclinic tides, should account for. This predicted signal was added back into the HFR data, and the resulting dataset was then averaged every 2 h.

b. *Assimilation results*

The assimilation of surface currents from the HFR is particularly important for the vorticity balance because this is the only direct measurement of the ocean surface currents. The main aspect that differentiates the experiments is whether or not the HFR radial velocities are filtered to remove the high frequencies. The outputs from the simulations are compared to the original data to determine their ability in reproducing the ocean state.

1) SLA AND SST

The use of raw HFR data (experiment A) results in larger differences in some regions, particularly in the lee (southwest) of the primary islands (Hawaii, Maui, and Oahu). This is related to the adjustments that the assimilation process performs to minimize the differences in the high-frequency signal between the model and the HFR data. In experiment B, the high-frequency signal is purely from the model prediction, meaning the assimilation experiments are fully capable of representing such variability when adjusting to the observed, low-frequency currents. The difference in the SLA representation between model results due to the treatment of the radial velocities is small (Table 1). The use of raw HFR radial velocities results in slightly smaller mean differences. All experiments well reproduce both the SLA and SST observations when compared to a similar system analyzed by Matthews et al. (2012). The root-mean-square difference (RMSD) between the model and observations for SST (SLA) for Matthews et al. (2012) was 0.5°C (0.1 m).

A particular improvement in the representation of the observed SLA and SST is observed in the lee side of the islands where large mesoscale variability is observed, as illustrated by the eddy kinetic energy map in Fig. 1c of Lumpkin and Flament (2013). Matthews et al. (2012) show this region presents overall larger errors, related to the increased mesoscale activity.

2) SURFACE RADIAL VELOCITIES

The RMSD maps of the low-frequency surface currents (48-h low-pass filtered) in Fig. 2 show that although the spatial distributions are slightly different, the assimilation of the radial velocities leads to smaller errors. Experiment A compares most favorably with the low-frequency HFR currents with an RMSD less than $4\,cm\,s^{-1}$ over most of the area covered by the radar. As shown in Table 1, experiment B, despite assimilating the low-frequency HFR currents exhibit, shows a 35% worse comparison with the low-frequency HFR as compared to experiment A. As would be expected, the worst comparison is for experiment C, where the HFR radials were not assimilated.

As mentioned before, because the model representation of the region can never perfectly reconstruct the factors that control the generation and propagation of the internal tides, the difference between the HFR and model experiments should be most pronounced in the high-frequency band above the inertial. Using a point located in the presence of both strong mean currents and significant baroclinic energy flux (approximately at 21.02°N, 158.23°W), we examine the time series of surface radial velocities for the HFR, and the simulation results are shown in Fig. 3. The assimilation of raw HFR data led to improvement in the model representation of both low- and high-frequency currents. The figure shows that the high-frequency variability present in both the model results and the observations are greater than inertial with

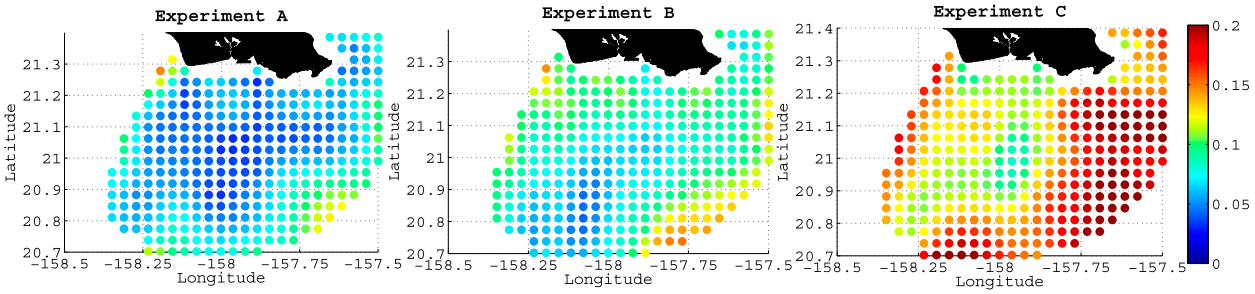

FIG. 2. Low-frequency (48-h low-pass filter) RMSD ($m\,s^{-1}$) between the HFR radial velocities and the results of the three experiments. The assimilation of the raw HFR data leads to considerably smaller RMSD.

most of this energy around the semidiurnal tides (M_2 and S_2).

To understand the accuracy of the experiments in representing the observed HFR velocities, cross spectra in relation to the HFR data are shown in Fig. 4a. All experiments are able to well represent the observed energy spectrum; however, the inclusion of the HFR radial velocities clearly improves the model solution. The M_2 phase shift between the observations and each experiment is found to be significantly reduced for experiment A: experiment A is −5.2 min, experiment B is −43.9 min, and experiment C is 29.0 min. When assimilating the HFR radials with the model-predicted high-frequency signals, M_2 arrived nearly 45 min early, which is worse than when not assimilating the HFR radials at all. Despite the potential differences between the generation and propagation of the baroclinic tides, it is favorable to use the observed HFR spectra to better simulate the results as the model uses this information to improve the stratification (the barotropic tidal forcing is not modified by the assimilation). These results are consistent with those found in Matthews et al. (2012).

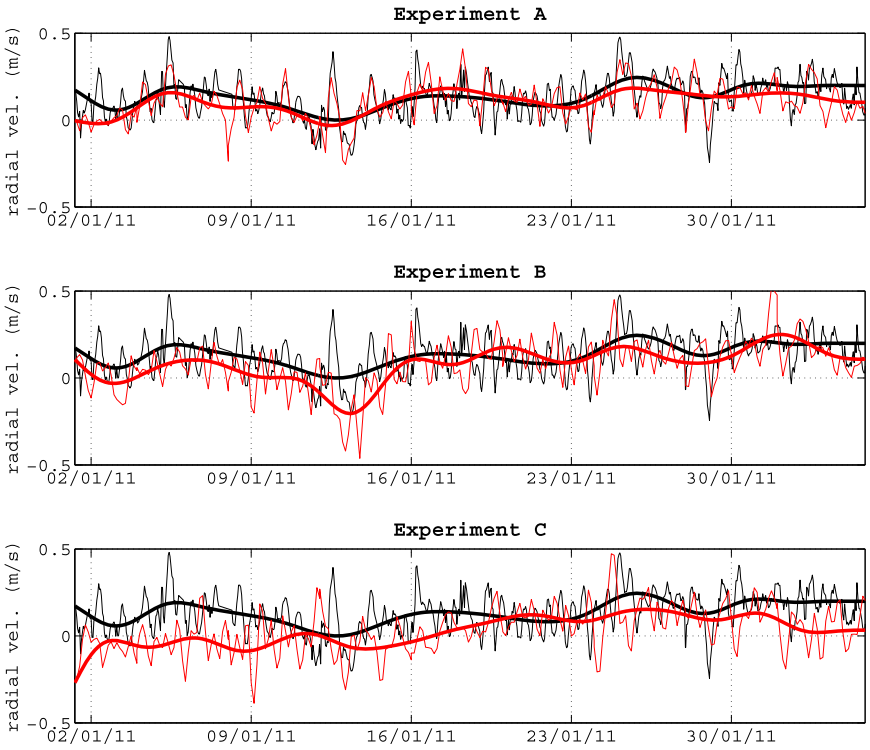

FIG. 3. Time series of radial surface currents ($m\,s^{-1}$) for a point south of the island of Oahu (21.02°N, 158.23°W) from the HFR (black) and model (red) for the three experiments. The thick lines show the low-frequency radial surface currents (48-h low-pass filter). Only approximately 1 month is shown to enable the visualization of the high-frequency variability.

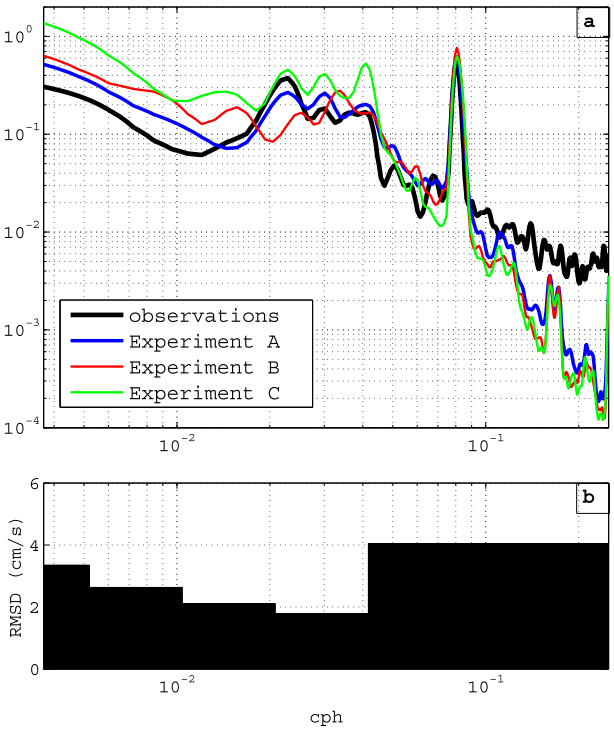

FIG. 4. (a) Spectra of the radial surface currents ($m^2 s^{-2}$) from the HFR and the results of the three experiments. The experiment with the assimilation of raw radial velocities (experiment A) shows energy levels closer to the observations. (b) RMSD ($cm s^{-1}$) between the reanalysis results and the HFR data for several period windows. Higher errors were observed for variability with the period under 1 day and between 16 and 64 days. The errors for every window were under 4.5 $cm s^{-1}$, close to the ≈3 $cm s^{-1}$ accuracy of the HFR.

These results are from the 1-month simulation used to compare the different strategies of HFR data assimilation, and based upon the three experiments, we selected experiment A (without filtering HFR data) as the basis to perform the 18-month reanalysis to examine the vorticity budget. Using this long reanalysis, we tested how well the reanalysis captures the surface currents as compared to the HFR data by examining the RMSD between the two at different spectral bands. Several different bandpass filters were applied to both the data and model results. The RMSD for each band was calculated and is presented in Fig. 4b. The highest RMSD are found for the currents with periods under 1 day and between 16 and 64 days. The periods under 1 day include errors due to the aliasing produced by undersampling the model output every 3 h (because of resource limits, the model output is saved every 3 h) and the minor phasing differences in the semidiurnal tidal currents. It is interesting to note that the period between 1 and 2 days, including the local inertial period, contains the smallest RMSD. The individual errors are below 4.5 $cm s^{-1}$, which is slightly more than the advertised precision of the HFR data (3 $cm s^{-1}$).

The results from the three experiments, and particularly the long comparison with the HFR data in Fig. 4, show the model is capably resolving the wide range of energy present in the system (from semidiurnal tides to mean flows). Using this 18-month reanalysis, we now aim to understand both the nature and control of the vorticity balance in the region.

4. Vorticity balance of the ocean surface

Vorticity plays a central role in geophysical fluid dynamics, with both atmospheric and oceanic large-scale circulations governed by the evolution of potential vorticity. Complex interactions between the ocean and atmosphere can be expressed through the flux of vorticity across the interface. In Hawaii, the presence of the high-altitude islands disrupts the local atmospheric circulation with direct consequences on the ocean surface, affecting the circulation pattern and heat distribution with important consequences from local to synoptic to climatic scales (Chavanne et al. 2002). The study of the vorticity balance provides a way to understand how local perturbations evolve to large-scale processes.

As shown in the previous section, the assimilation of raw HFR radial velocities was the leading factor for the improvement of the simulated ocean surface currents, and its impacts are found in unobserved, remote parts of the domain. Because 4D-Var uses the model dynamics to determine covariance, unobserved regions of the domain are also adjusted in balance by the observations. The assimilation of the HFR data in the region south of Oahu impacts the ability of the rest of the domain to maintain the flow observed near the island.

The time-averaged ocean surface relative vorticity derived from the reanalysis (Fig. 5) resembles the mean picture from Lumpkin and Flament (2001), with cyclonic vorticity dominant to the north and anticyclonic vorticity dominant to the south of 19.5°N. However, detailed differences between the cyclonic and anticyclonic vorticity regions are shown in Fig. 5. Regions of anticyclonic vorticity emanate from the southern end of the smaller island wakes, disrupting the mostly cyclonic vorticity region. The anticyclonic vorticity band centered at 18.5°N is zonally consistent. Vorticity is generally stronger closer to the islands and weakens with distance from the wake region, but the reanalysis contains a secondary maximum of both cyclonic and anticyclonic vorticity to the south of the island of Kauai. This secondary wake was also observed by Xie et al. (2001) 300 km downwind from the islands using satellite data, and it is present in the mean eddy kinetic energy (EKE) maps obtained from model

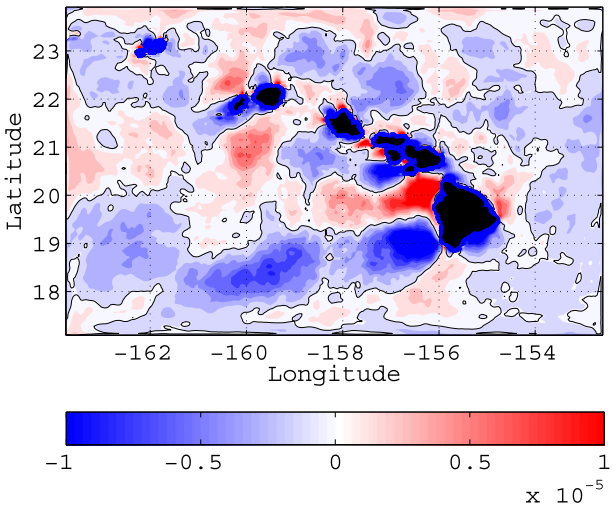

FIG. 5. Mean ocean surface vorticity (s^{-1}) derived from the model results. A dominance of cyclonic (anticyclonic) vorticity to the north (south) of the 19.5°N parallel is observed. The region with predominance of cyclonic vorticity originating from the island of Hawaii interacts with the wakes from the other islands, while the anticyclonic vorticity propagates west-southwest without further interaction with the island wakes.

simulations by Calil et al. (2008). Our results indicate the secondary wake is related to the wake of Oahu and energy passing through the channel that separates the islands of Oahu and Kauai.

Using the surface model upper layer as defined in the appendix, it is possible to estimate the contribution of different forcing terms to the vorticity balance, calculated at each model grid point by the combination of advection, divergence, wind forcing, and deeper ocean forcing/sink, given by

$$\frac{\partial\zeta}{\partial t} = \underbrace{-\left(\mathbf{u}\frac{\partial\zeta}{\partial x}+\boldsymbol{v}\frac{\partial\zeta}{\partial y}\right)}_{\text{Advection}} \underbrace{-\boldsymbol{v}\beta}_{\text{Beta}} \underbrace{+(\zeta+f)\left(\frac{\partial\mathbf{u}}{\partial x}+\frac{\partial\boldsymbol{v}}{\partial y}\right)}_{\text{Divergence}} + \underbrace{\left(\frac{\partial F^y}{\partial x}-\frac{\partial F^x}{\partial y}\right)}_{\text{Wind stress curl}} + \underbrace{\left(\frac{\partial F_b^y}{\partial x}-\frac{\partial F_b^x}{\partial y}\right)}_{\text{Ocean stress curl}}, \quad (1)$$

where ζ is the ocean surface relative vorticity, $(\mathbf{u}, \boldsymbol{v})$ are the daily mean zonal and meridional ocean current velocities, f is the Coriolis parameter, β is the meridional gradient of f, (F_x, F_y) are the zonal and meridional wind forcing defined as $F = \tau/\rho_0$, the wind stress scaled by the ocean mean density, and (F_b^x, F_b^y) are the zonal and meridional stresses between the surface layer and the model layer below. The stress F_b can be approximated by

$$\frac{F_b}{\rho_0} \approx A_{kv}\frac{\partial^2\mathbf{u}}{\partial z^2}, \quad (2)$$

where A_{kv} is the Mellor–Yamada level-2.5 closure vertical mixing coefficient for momentum (Mellor and Yamada 1982) internally calculated by ROMS and $\mathbf{u}$ is the horizontal velocity. A fourth-order central difference scheme was used to calculate the spatial partial derivatives. The beta term was found to be negligible and is not considered for the remainder of the discussion.

Several authors have studied the surface vorticity balance in different water bodies. For example, the vorticity balance expressed in Eq. (1) is similar to the method Schwab and Beletsky (2003) used to calculate the depth-integrated vorticity in Lake Michigan. Their internal pressure term is neglected in our study because we have a surface layer with nearly constant thickness, and their bottom stress term is similar to our ocean forcing term that includes the stress between the surface layer and the ocean below it. These authors conclude that the wind stress curl and the baroclinicity are primarily responsible for the observed vorticity in the lake; however, other dynamical processes become important in open water. Thomas (2005) studied the interaction between the wind and ocean fronts and observed that the potential vorticity of surface waters is modified by both frictional and diabatic processes until the fluid is subducted into the ocean interior. Although they considered the same processes, special emphasis was given to the wind frictional effects. Murray et al. (2001) show that the advection of vorticity into/out of the domain can be important for its balance in large time scales. Using results from a high-resolution numerical model experiment, the authors relate the interannual variability in the ocean surface vorticity to the variability in the atmosphere and the advection due to coastal Kelvin waves entering the Gulf of Alaska.

In Hawaii, the transference of vorticity from the wind curl in the wake of the islands to the ocean surface circulation is an important process affecting the entire tropical Pacific climate. As described by Xie et al. (2001), this wind curl gives rise to the HLCC that advects warmer water from the west, modifying the regional ocean–atmosphere fluxes and the winds in the marine atmospheric boundary layer (MABL). Following these authors, the broader wake that forms downwind after quick dissipation of the individual islands wakes is assumed to force Rossby waves, establishing the HLCC. Sasaki et al. (2013) used an ocean–atmosphere coupled simulation to verify that the atmospheric response to the warm HLCC is responsible for modifying the ocean surface current and to accelerate (decelerate) the southern (northern) portion of the HLCC. The mechanisms behind the transition from the islands to this broader wake are not clear.

Our results show a pattern similar to the one described by Xie et al. (2001). The vorticity budget averaged over

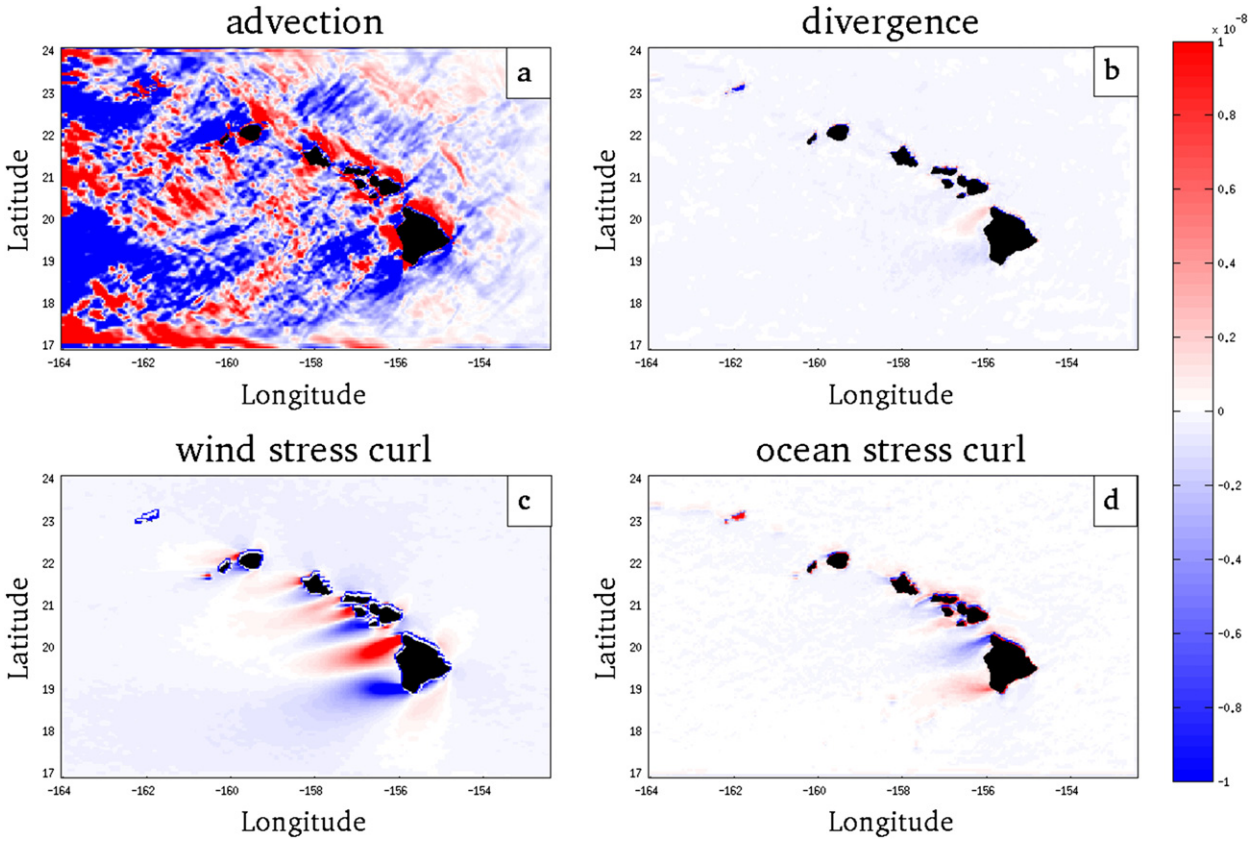

FIG. 6. Time-averaged terms of Eq. (1) (s^{-2}). The mean map of the (a) advection shows the influence of the canonical surface circulation on the vorticity distribution. The small contribution of the (b) divergence is a consequence of the time mean that masks important instantaneous contributions. The maps for the (c) wind stress curl and (d) ocean stress curl show the dominance of the wake of the trade winds on the lee of the islands and the consequent transference of this vorticity downward, respectively.

the 18-month reanalysis is shown in Fig. 6. The average contribution from the wind stress curl shows the clear influence of the islands on the trade winds. Nearly constant positive (negative) contributions of the wind stress curl (Fig. 6c) in the northwest (southwest) side of the islands is observed, reflecting the dominance of the trade winds in time. Similarly, the ocean stress curl (Fig. 6d) is responsible for locally conveying part of the vorticity introduced by the winds to the deeper layers. Although the spatial pattern and order of magnitude of these two terms are similar, the difference between them is not zero; therefore, part of the vorticity introduced by the winds to the ocean surface is not locally transferred downward. The contribution from the ocean stress curl includes processes not explicitly resolved in Eq. (1) such as the surfacing of baroclinic tides. This residual is found to be ≈7% for the regional integrated balance.

While the wind stress curl term is dominant in the immediate lee of the islands, the presence of a well-organized mean circulation and the propagation of perturbations indicate that the dominant contribution to vorticity is the advection away from the islands' wake. The spatial pattern of the advection term (Fig. 6a) is similar to the vorticity map presented by Lumpkin and Flament (2001). The higher resolution of our reanalysis reveals advected anticyclonic vorticity through the channel separating Oahu and Kauai where the dominant background vorticity is cyclonic. Comparing the averaged terms in Fig. 6 with the mean ocean surface vorticity in Fig. 5, the wind forcing cannot be responsible for the secondary wake in vorticity. Since these results include only an oceanic component, no coupled processes such as the one discussed by Xie et al. (2001) and Sasaki et al. (2013) are present. Our reanalysis shows the ocean surface vorticity away from the islands is dominated by the advection.

In fact, as demonstrated by Kersale et al. (2011) using an ocean numerical model and different sets of wind sources, the wind stress curl is a key factor in the formation of the mesoscale eddies observed in the lee of the Hawaiian Islands. These authors show how the wind stress variations in the lee of the islands drive divergent and convergent Ekman transports in the ocean upper

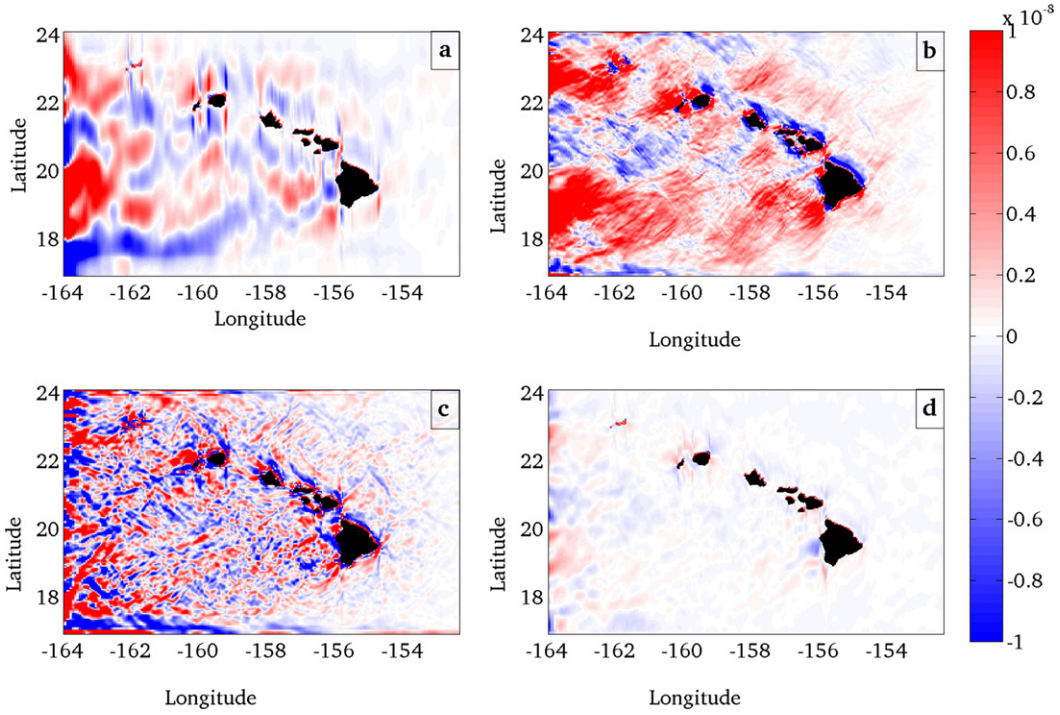

FIG. 7. Time-averaged maps (18 months) of the terms of Eq. (5) that show the spatial separation of the advection term of Eq. (2) into (a) mean flow ($\overline{\mathbf{u}}\nabla\overline{\zeta}$), (b) eddy contribution ($\mathbf{u}'\nabla\zeta'$), (c) mean advection of eddy vorticity ($\overline{\mathbf{u}}\nabla\zeta'$), and (d) eddy advection of mean vorticity ($\mathbf{u}'\nabla\overline{\zeta}$).

layer. They point to the combined effect of the wind stress curl, inflow current, and topography as equally important for the formation of the eddies. Our results emphasize the importance of this input of vorticity because of the wind stress curl in the wake of the islands and its westward advection by the currents. We do not distinguish any coherent advection of vorticity south of the island of Hawaii.

Being a second-order derivative, the vorticity gradient field is highly sensitive to noise that can be seen in Fig. 6a. To approach this problem and distinguish between the contribution of the mean flow and the eddies, we decompose the velocity into large- and small-scale fields:

$$\mathbf{u} = \overline{\mathbf{u}} + \mathbf{u}', \tag{3}$$

where a low-pass spatial filter with a cutoff length scale of 90 km was used separate the large-scale currents $\overline{\mathbf{u}}$ from the meso- and submesoscale eddies $\mathbf{u}'$. Applying Eq. (3) to the advection term of Eq. (1), we find

$$\underbrace{\mathbf{u}\nabla\zeta}_{\text{Total advection}} = \underbrace{\overline{\mathbf{u}}\nabla\overline{\zeta}}_{\text{Large scale}} \underbrace{+\,\mathbf{u}'\nabla\zeta'}_{\text{Eddies}} \underbrace{+\,\mathbf{u}'\nabla\overline{\zeta} + \overline{\mathbf{u}}\nabla\zeta'}_{\text{Interaction terms}}. \tag{4}$$

As shown in Fig. 7, most of the incoherent structure comes from the interaction between the large-scale currents and the eddy vorticity ($\overline{\mathbf{u}}\nabla\zeta'$) (Fig. 7c), while the eddy advection of large-scale vorticity ($\mathbf{u}'\nabla\overline{\zeta}$) is an order of magnitude smaller than the other terms. We will concentrate on the analysis on the large-scale and eddy terms of Eq. (4).

The influence of the canonical circulation and large-scale (>90 km) processes transporting the vorticity introduced by the northeasterly winds is observed in the large-scale term ($\overline{\mathbf{u}}\nabla\overline{\zeta}$) (Fig. 7a). Two regions of negative advection correspond to HLC and NEC, connecting the wake on the lee of Hawaii with the western boundary of the domain. The presence of the HLCC is evident by a band of positive advection around 19.5°N that corresponds to the boundary between the regions dominated by cyclonic and anticyclonic vorticity in Fig. 5. This pattern agrees with the ideas for the generation of the HLCC proposed by Chavanne et al. (2002). These authors show how a simple Sverdrup balance excited by the wind stress curl in the wake of the island of Hawaii results in two counterrotating gyres that give rise to the HLCC.

Because strong transient structures are frequent in the lee of the islands, the mean circulation does not describe the highly variable vorticity balance of the surface layer. While the contribution of the wind remains almost constant, the advection and divergence terms (Figs. 6a,b) are

highly variable and associated with ocean meso- and submesoscale eddies. The eddy advection term ($\mathbf{u}'\nabla\zeta'$) in Fig. 7b shows a westward advection of anticyclonic vorticity to the south and cyclonic vorticity to the north of the HLCC mean position. While the region dominated by anticyclonic vorticity extends uninterrupted from the wake of Hawaii to the west, the region dominated by cyclonic vorticity is perturbed by the wake of the other islands. In addition, the advection of vorticity to the NHRC on the windward side of the islands (northeast) is evident, as described by Qiu et al. (1997).

The large-scale advective term is the only one to present a meaningful correlation with the time variation of the surface vorticity over the 95% significance level, emphasizing its dominance on the balance [Eq. (2)]. The mean currents have positive correlation values in the HLCC and negative values (anticorrelation) over the HLC and NEC. The correlations of the vorticity variation with the eddy advection term are scattered across the domain, reflecting the high spatial and temporal variability of the eddy vorticity.

The winds, dominated by the trades throughout the year, input vorticity to the ocean surface in the lee of the islands. This wake is observed for all the main islands, but it is particularly important to the lee of the islands of Hawaii and Maui. Part of this vorticity, about 44%, is locally transferred to the ocean interior by the ocean stress curl term. The cyclonic vorticity that is not lost to the interior is advected westward, being partly responsible for what Xie et al. (2001) called a broader wake. Although the divergence acts as a sink for this positive vorticity through vortex stretching, this is very small compared to the advection. The mechanism behind the propagation of the anticyclonic vorticity is less clear. As described by Calil et al. (2008), while the mesoscale cyclones are confined to the lee of the islands and subjected to further interaction with the winds and dissipation processes, the anticyclones propagate west-southwest, and their signal can be observed over 4000 km away from Hawaii. While the eddy advection terms show a pattern coherent with the surface distribution of both cyclonic and anticyclonic vorticity (Fig. 5), only the large-scale advection is significantly correlated with the vorticity variability. Since both eddy and large-scale advection terms have the same order of magnitude, it remains a question as to how the eddies affect the large-scale vorticity. To examine this issue, we explore the spatial scales involved in the vorticity balance.

a. Spatial scales of the vorticity balance terms

We initially consider only the large-scale and eddy components of the advection terms ($\mathbf{u}\nabla\zeta = \overline{\mathbf{u}}\nabla\overline{\zeta} + \mathbf{u}'\nabla\zeta'$). Zonal wavenumber spectra of the surface vorticity were calculated for a region in the lee of Hawaii between 18° and 20.7°N, and we find that for the region vorticity is at longer scales, confined to the southern part of the domain at the boundary between the HLCC and the NEC. The other area that shows evidence of longer scales is at the boundary between the HLCC and HLC; however, this is less than half of the amplitude as the southern band.

The meridional distribution of the vorticity spectra indicates different phenomena are influencing the ocean surface vorticity as we move west from the islands. Figure 8 shows the wavenumber spectra for each term of Eq. (1) at two zonal sections (18.2°N, NEC/HLCC; 20.3°N, HLCC/HLC). The difference in the wind stress curl contribution indicates the influence of the wake of the other islands on the 20.3°N section that leads to higher spectral densities. Only the advection term shows higher spectral density for the southern section, and this difference is concentrated in the lower wavenumbers. This indicates the large-scale processes are important in the southern part of the domain and absent in the northern part. First baroclinic mode Rossby waves are the main process for adjustment of the oceanic vorticity to the wind forcing in the large-scale circulation. In fact, Xie et al. (2001) found the observed continuous westward extension of the HLCC indicates Rossby wave propagation. Hovmöller diagrams of the ocean surface vorticity along the zonal sections at 18.2° and 20.3°N (Fig. 9), centered along the regions of anticyclonic and cyclonic vorticity, respectively, show a westward propagation pattern for the anticyclonic vorticity that is not evident for the cyclonic case. A phase speed of approximately 5.2 km day^{-1} is found for the advection of anticyclonic vorticity, which is roughly 3 times the averaged ocean surface currents for the area. This value agrees with the expected phase speed for first baroclinic mode Rossby waves at this latitude (Chelton and Schlax 1996).

Since there is no absolute definition for the wavenumbers covering submesoscale processes, we characterize it by the length scales where the dynamical balance changes from geostrophy to ageostrophy. In a practical manner, submesoscale is therefore defined by wavelengths smaller than half the first baroclinic mode Rossby deformation radius for the region ($\leq$40 km).

For length scales smaller than 100 km, the advection spectra presents a k^{-3} slope. To analyze the interaction of the meso- and submesoscale eddies with the large-scale flow, the zonal spectra of the advection interaction terms of Eq. (4) along 20.3°N are presented in Fig. 10a. The same k^{-3} slope is observed for ($\mathbf{u}'\nabla\overline{\zeta}$) at length scales between 16 and 100 km, while ($\overline{\mathbf{u}}\nabla\zeta'$) presents a much steeper slope ($\approx k^{-8}$) that abruptly flattens around 50 km. This indicates the influence of the eddy velocities over the large-scale vorticity advection is

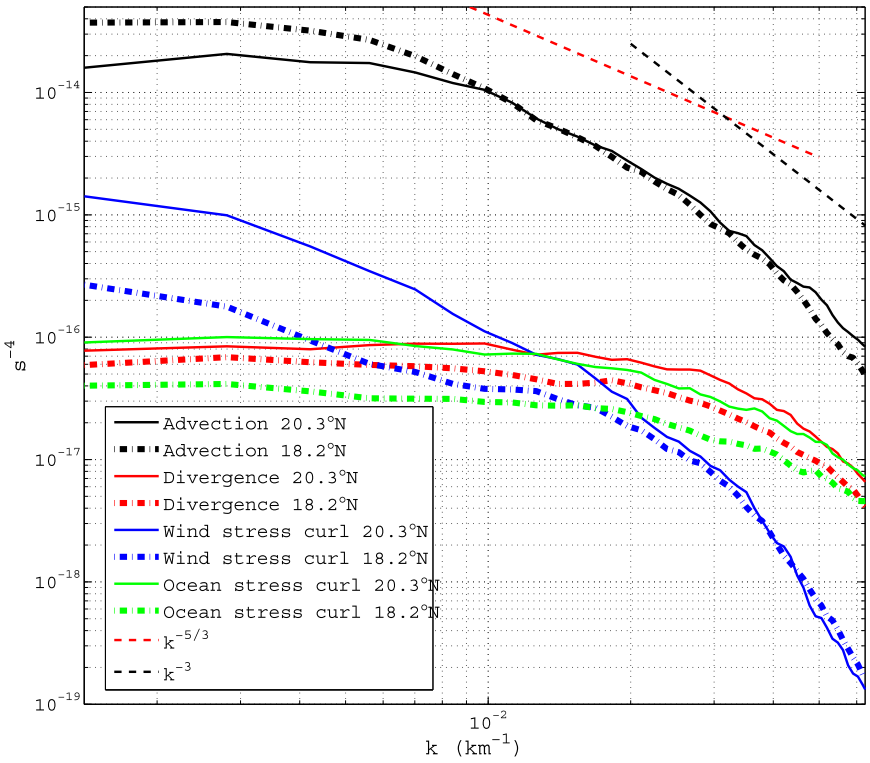

FIG. 8. Wavenumber spectra of the vorticity balance terms for two zonal sections in the lee of Hawaii at 20.3° and 18.2°N. The advective term presents higher spectral density for the 18.2°N section, indicating the influence of a larger-scale process. The slope of the advection term spectra suggests a cascade of vorticity from the submesoscale toward the mesoscale and large scales.

responsible for the suggested cascade. The difference in the magnitude of the two terms is because of the difference in the gradient of the large scale and eddy vorticity. The section at 18.2°N presents the same pattern (not shown).

The spectrum of the reanalysis SSH (Fig. 10b) for this same zonal section (20.3°N) presents a k^{-5} slope. This is steeper than found by Xu and Fu (2011) using altimetry data, but consistent with the law expected from quasigeostrophic turbulence (Smith and Vallis 2001). In a quasigeostrophic regime, the mesoscale tends to dominate the energy spectra cascading energy toward the large scale. According to Molemaker et al. (2010), in such a regime the flow is essentially balanced and nondivergent, while unbalanced motions are essential in establishing dissipation by means of a forward energy cascade. Quoting these authors, they state, ''As expected from geostrophic turbulence theory, the balanced motions provide an inverse energy cascade toward larger scales and contribute little energy dissipation in the interior region of the flow'' (Molemaker et al. 2010, p. 62). This is true for dynamical systems with small Rossby numbers (Ro), while a forward cascade toward dissipation is dominant in systems characterized by weak rotation and large Ro (e.g., Waite and Bartello 2006).

The spectra for the zonal and meridional components of the surface velocity (Fig. 10c) show a k^{-4}, $k^{-3.5}$ slope, steeper than the $\approx k^{-3}$ spectrum observed for the surface velocities by Sasaki and Klein (2012). These spectra suggest the local dynamics is characterized by a nonlinear regime with a decay in the energy levels toward the smaller scales. Capet et al. (2008) describe the shoaling of the spectrum at wavenumbers greater than the mesoscale spectral peak as a defining characteristic of the submesoscale transition, with a k^{-2} law for the velocity spectrum extending as far as the dissipation range at high wavenumbers. Their analysis and the associated forward energy spectrum concentrated in spatial scales of 10 km and smaller and excluded the region within 50 km from the coast. Because of the grid resolution, the reanalysis discussed here is able to properly resolve spatial scales larger than 16 km. Therefore, the definition of submesoscale in the present work does not cover the spectral region detailed by Capet et al. (2008). The contribution from the submesoscale in the reanalysis results is particularly important close to the leeward coast

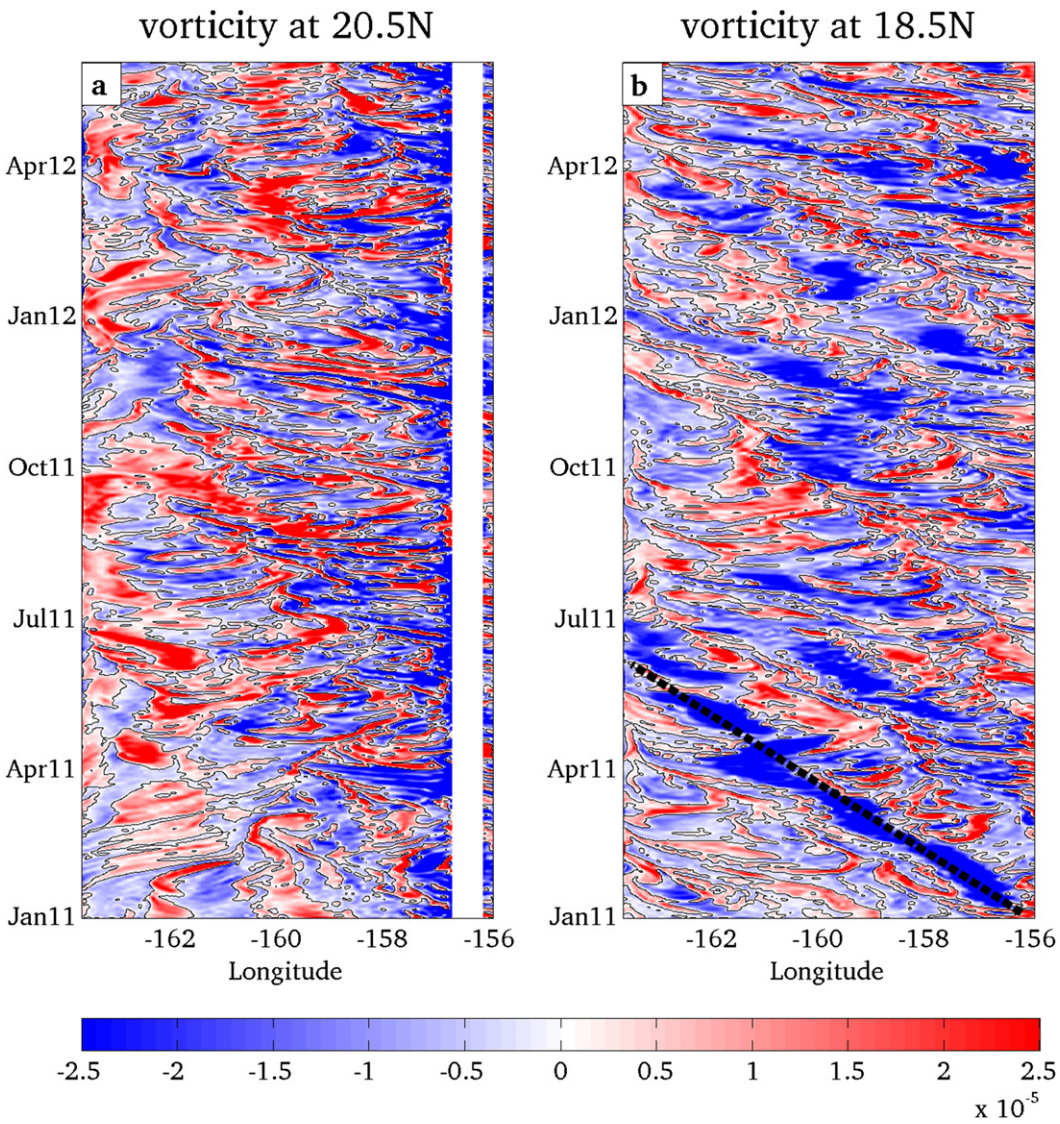

FIG. 9. Hovmöller diagrams of the ocean surface vorticity along the parallels of (a) 20.3°N and (b) 18.5°N, corresponding to the center of the regions dominated by cyclonic and anticyclonic vorticity, respectively. A wavelike propagation is observed for the anticyclonic vorticity pulses, exemplified by the black dashed line. The same is not true for the cyclonic vorticity.

of Hawaii, where ageostrophic instability is particularly important (Fig. 11; see next section). Therefore, the importance of ageostrophy and the steep and constant slope of the spectra in Fig. 10 across meso- and submesoscale (≤40 km) wavenumbers with an abrupt flattening toward larger scales suggest an inverse cascade that covers the smaller scales resolved by the reanalysis (≈16 km).

b. *Ageostrophic anticyclonic instability*

The results show that neither the wind nor ocean stress curls are relevant away from the immediate wind wake of the islands. In the region dominated by the cyclonic vorticity, a strong interaction with the wakes of the other islands is found. This is not the case for the band of anticyclonic vorticity. Chavanne et al. (2010) estimated the subinertial vorticity balance of an anticyclone in the lee of Oahu from gridded surface currents estimated from HFR measurements and QuikSCAT wind observations between September 2002 and May 2003. Similar to our modeled results, they used snapshots of their vorticity balance equation terms to deduce that the wind stress curl is the main factor for vorticity growth on the southwest of Oahu. They explain the decay of the absolute vorticity after a warmup period of the observed eddy through instability processes; however, their results

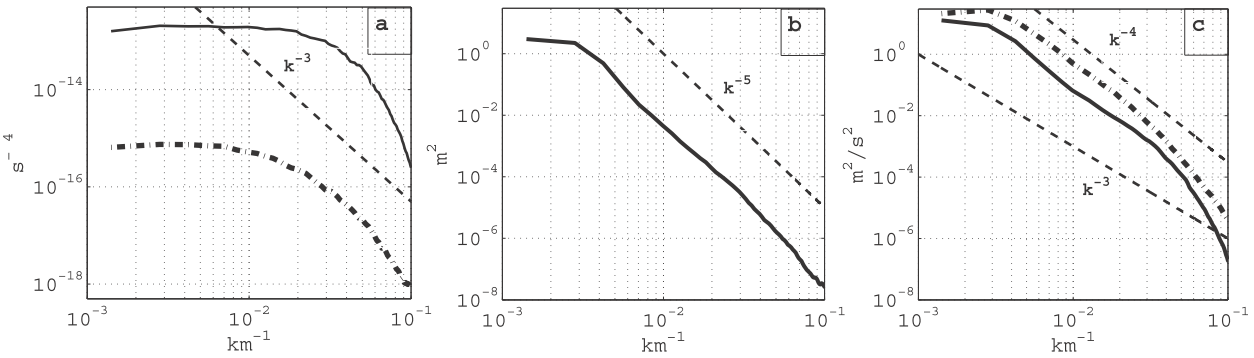

FIG. 10. (a) Zonal wave number spectra at 20.3°N of the interaction between scales terms of the advection. The continuous curve corresponds to the $(\bar{\mathbf{u}}\nabla\zeta')$ and the dashed curve corresponds to the term $(\mathbf{u}'\nabla\bar{\zeta})$. The dashed–dotted line shows a k^{-3} slope. For the same section, (b) the wavenumber spectra of SSH and (c) the wavenumber spectra of the zonal (solid line) and meridional (dashed–dotted line) velocity components are shown. The spectrum slopes are consistent with an energy cascade from the submesoscale and mesoscale toward the larger scales.

are not conclusive because of the lack of in situ data of the water column. In the present study, the important contribution of meso- and submesoscale eddies to the mean vorticity balance indicates that ageostrophic dynamics is relevant. The reanalysis permits us to calculate the ageostrophic anticyclonic instability (AAI) criterion, as defined by Chavanne et al. (2010) following Molemaker et al. (2005):

$$f(f+\zeta+\sigma)<0, \tag{5}$$

where $\sigma = [(\partial\mathbf{u}/\partial x - \partial\boldsymbol{v}/\partial y)^2 + (\partial\boldsymbol{v}/\partial x + \partial\mathbf{u}/\partial y)^2]^{1/2}$ is defined as the strain rate. The time mean of AAI from the reanalysis is shown in Fig. 11 and reveals that this is an important process for the sink of anticyclonic vorticity in the strong wake in the southwest of both Hawaii and Maui. Comparing the criterion map to the mean vorticity of the ocean surface (Fig. 5), it is clear that regions with strong negative (anticyclonic) vorticity coincide with regions of negative AAI indices. It is interesting to note the presence of a secondary region where the AAI criterion indicates instability detached from the island wakes to the south of the island of Kauai. This region is similar to the maximum EKE observed in model simulations by Calil et al. (2008), which the authors associated to ageostrophic processes. Although the AAI map reinforces this hypothesis, the small values indicate that on average the instability is weak in this region.

5. Conclusions

A model reanalysis is used to analyze the ocean surface vorticity balance in the Hawaii region. This reanalysis is built from an 18-month integration combining all available data with the ROMS model via 4D-Var data assimilation. A modification of the ROMS model *s*-coordinate system is used to better represent the ocean surface variability by applying a quadratic form to the typically linear σ function. This approach leads to smaller and consistent depths of the surface layer in simulation domains with large bathymetric variations, and it provides a better representation of the SST diurnal cycle and ocean surface circulation. Three experiments with different treatment for the assimilated HFR data are performed. The assimilation of the raw HFR radial velocities results in smaller error compared to the observed surface velocities and reduced SLA RMSD in remote regions of the domain. A particular good performance was observed for frequencies around the local inertial period, with RMSD within the range of the sensor accuracy. The

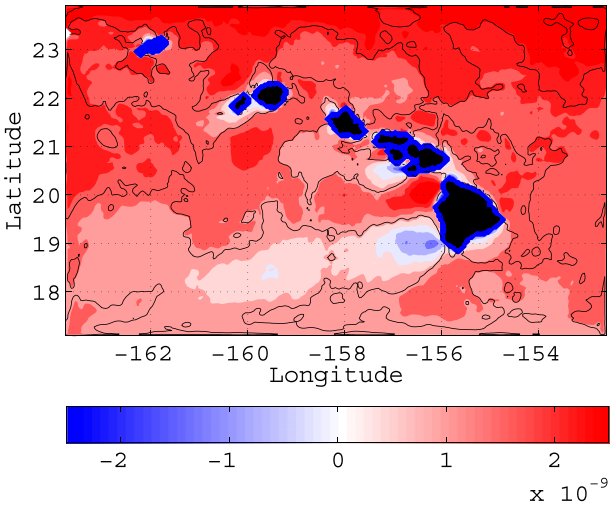

FIG. 11. AAI criterion, showing areas where this process leads to a cascade of vorticity to smaller scales prone to dissipation. The zero relative vorticity contours shown in black demonstrate this property dominates the AAI criterion.

direct influence of the wind stress curl on the surface vorticity balance is restricted to the wake region in the leeward coasts of the islands with particular contribution from the wake of the islands of Hawaii and Maui. About 44% of the vorticity introduced by the winds is locally transferred to the ocean interior. The advection is the dominant term transporting the vorticity westward. Although both the large-scale and eddy contributions to the advection have the same order of magnitude, only the large-scale component is significantly correlated to the variability of the total ocean surface vorticity. This can be interpreted as the influence of the large-scale canonical circulation and long Rossby wave variability on the total vorticity. The secondary wake observed by previous authors is present in the reanalysis results, although these phenomena have been previously related to an ocean–atmosphere coupling mechanism. Our reanalysis suggests that the secondary wake is associated with the advection of vorticity from the lee of the smaller islands.

The spectral analysis suggests an inverse cascade of eddy vorticity from meso- and submesoscales toward the large scale, where the submesoscale was defined by half the first baroclinic mode Rossby deformation radius ($\leq$40 km). Previous studies show a forward cascade toward dissipative scales for eddies $O(10)$ km. Although this inverse cascade was observed throughout the lee of the islands, it leads to different levels of large-scale vorticity between the northern (dominated by cyclonic vorticity) and southern (dominated by anticyclonic vorticity) parts of the domain. While in the north there is interaction with the smaller islands' wakes that are implicitly taken into account by the advection term, the same is not true for the region dominated by anticyclonic vorticity. Our results agree with the existing hypothesis that baroclinic Rossby waves are responsible for the westward propagation of the vorticity in this region. The propagation velocity of the anticyclonic vorticity pulses originated in Hawaii, and it is in accordance with the expected phase velocity for a first baroclinic mode Rossby wave at this latitude.

Since the transfer of vorticity to the ocean interior, vortex stretching, and interaction with the wind are small, other mechanisms are examined as a sink of vorticity. The anticyclonic instability appears to play a role in cascading energy to dissipative scales.

This study contributes to our understanding of how the vorticity input from the winds in the Hawaiian Islands drives the ocean surface circulation, defining a pattern that influences the entire tropical Pacific. Although a coupled process as observed by Sasaki et al. (2013) is important for the intensification of the HLCC, the wind wake by the islands alone is capable of producing the observed vorticity distribution and gives rise to the Rossby waves responsible for setting up the tropical Pacific circulation.

Acknowledgments. We thank the editor, Dr. William Kessler, and the two anonymous reviewers for valuable contributions to the manuscript. Dr. Souza was supported on NOAA Grant NA07NOS4730207. Dr. Powell was supported by ONR Grant N00014-09-1-0939.

APPENDIX

Modification of the Vertical Coordinate

Stretching functions $C(\sigma)$ in ROMS provide a mapping of water depth into a nondimensional coordinate varying between 0 at the surface and -1 at the bottom. The two most popular schemes were defined by Shchepetkin and McWilliams (2005) and are hereinafter called VS2 and VS4. In both cases, $C(\sigma)$ is calculated with respect to the vertical coordinate σ, and the surface and bottom control parameters θ_S and θ_B, respectively. The obtained stretching functions are continuous with respect to θ_S and θ_B as their values approach zero.

Currently, two transformation options are available in the ROMS model to obtain the layer depths as function of the free-surface elevation $\eta(x, y, z)$, the unperturbed water depth h (x, y), the fractional vertical stretching coordinate σ ranging from $-1 \leq \sigma \leq 0$, the nondimensional vertical stretching function $C(\sigma)$ ranging from $-1 \leq C(\sigma) \leq 0$, and a positive thickness controlling the stretching h_c.

To capture the strong diurnal signals in SST and the semidiurnal reversals of the surface currents due to baroclinic tides, constraining the spatial variation of the surface layer thickness is important to improve the representation of ocean surface properties in the Hawaii simulations. This requires a fixed, small value for the σ coordinate of the model surface layer. A quadratic Legendre polynomial is used to obtain the σ values of the remaining layers, once their first and last layers values are also known (-1 and 0, respectively):

$$\sigma(k) = -\frac{k^2 - 2kN + k + N^2 - N}{N^2 - N} - \omega\frac{k^2 - kN}{1 - N}, \qquad \text{(A1)}$$

where N is the total number of layers, k is the layer number ($1 \leq k \leq N$), and ω is the value at the surface layer ($k = N - 1$). In the present study, a value of -0.01 was chosen for ω. It is important to emphasize that the new function for σ will impact all model layers and the representation of the ocean interior.

The quadratic σ allows higher resolution near the surface that cannot be achieved by the linear function.

Tests conducted with different θ_S values indicate that, even with its maximum recommended value of 10 (Shchepetkin and McWilliams 2009), a large variation in the model final layer is still observed for both VS2 and VS4 inside our model domain. Using $\theta_S = 6.5$ and $\theta_B = 4$, values used for all the simulations in the present study, and considering the ocean at rest, the quadratic σ results in ocean surface layer thicknesses between 0.5 and 2.5 m. However, this finer surface discretization comes at the cost of the loss of resolution near the bottom, although no deterioration of the representation of bottom currents or increase of the pressure gradient errors (PGE) were observed.

To assess the performance of the new function for the vertical coordinate, three experiments using linear and quadratic σ with different stretching functions were designed; two used the traditional linear σ and either the piecewise stretching function (VS2) or the continuous, double stretching function (VS4). The third experiment used the combination of the new quadratic function for σ and the VS4, defined hereinafter as VS5. All experiments were run for the month of January 2011.

The VS5 scheme presented higher SST variability as a consequence of the smaller mean surface layer thickness. The mean spectrum (not shown) shows that this larger variability is concentrated in the high frequency, with particular contribution of the diurnal cycle. Even in the deep regions of the model domain, the diurnal cycle of the SST is stronger in the VS5 scheme. This difference between the three schemes is reduced in lower frequencies, becoming negligible for time scales longer than 48 h.

The momentum flux is also affected. Impacts on the surface velocities are expected as thinner layers respond quicker to wind stress variations. To analyze such effects, ≈30 days of radial velocities obtained from the HFR located at Kalaeloa (≈21.3°N, 158°W), between 26 January 2011 and 7 March 2011, were compared to the simulation results. The model currents were projected into radials similar to the radar data, and cross spectra were calculated. Although all the vertical schemes fail to reproduce the high-frequency energy levels observed in the radar data, the VS5 scheme produces more energy at high frequencies than the other two, which can be attributed to wind and tidal forcings. A particularly good agreement in spectral power between the VS5 simulation results, and the HFR is observed for the diurnal frequency.

REFERENCES

Bleck, R., 2002: An oceanic general circulation model framed in hybrid isopycnic Cartesian coordinates. *Ocean Modell.,* **4,** 55–88, doi:10.1016/S1463-5003(01)00012-9.

Calil, P. H. R., K. J. Richards, Y. Jia, and R. R. Bidigare, 2008: Eddy activity in the lee of the Hawaiian Islands. *Deep-Sea Res. II,* **55,** 1179–1194, doi:10.1016/j.dsr2.2008.01.008.

Capet, X., J. C. McWilliams, M. J. Molemaker, and A. F. Schepetkin, 2008: Mesoscale to submesoscale transition in the California Current System. Part III: Energy balance and flux. *J. Phys. Oceanogr.,* **38,** 2256–2269, doi:10.1175/2008JPO3810.1.

Carter, G. S., and Coauthors, 2008: Energetics of M2 barotropic-to-baroclinic tidal conversion at the Hawaiian Islands. *J. Phys. Oceanogr.,* **38,** 2205–2223, doi:10.1175/2008JPO3860.1.

Chavanne, C., P. Flament, R. Lumpkin, B. Dousset, and A. Bentamy, 2002: Scatterometer observations of wind variations induced by oceanic islands: Implications for wind-driven ocean circulation. *Can. J. Remote Sens.,* **28,** 466–474, doi:10.5589/m02-047.

——, ——, and K. W. Gurgel, 2010: Interactions between a submesoscale anticyclonic vortex and a front. *J. Phys. Oceanogr.,* **40,** 1802–1818, doi:10.1175/2010JPO4055.1.

Chelton, D. B., and M. G. Schlax, 1996: Global observation of oceanic Rossby waves. *Science,* **272,** 234–238, doi:10.1126/science.272.5259.234.

Cummings, J. A., 2005: Operational multivariate ocean data assimilation. *Quart. J. Roy. Meteor. Soc.,* **131,** 3583–3604, doi:10.1256/qj.05.105.

Dushaw, B. D., B. M. Howe, B. D. Cornuelle, P. F. Worcester, and D. S. Luther, 1995: Barotropic and baroclinic tides in the central North Pacific Ocean determined from long-range reciprocal acoustic transmissions. *J. Phys. Oceanogr.,* **25,** 631–647, doi:10.1175/1520-0485(1995)025<0631:BABTIT>2.0.CO;2.

Egbert, G. D., and S. Y. Erofeeva, 2002: Efficient inverse modeling of barotropic ocean tides. *J. Atmos. Oceanic Technol.,* **19,** 183–204, doi:10.1175/1520-0426(2002)019<0183:EIMOBO>2.0.CO;2.

Eriksen, C. C., T. J. Osse, R. D. Light, T. Wen, T. W. Lehman, P. L. Sabin, J. W. Ballard, and A. M. Chiodi, 2001: Seaglider: A long-range autonomous underwater vehicle for oceanographic research. *IEEE J. Oceanic Eng.,* **26,** 424–436, doi:10.1109/48.972073.

Janeković, I., and B. Powell, 2012: Analysis of imposing tidal dynamics to nested numerical models. *Cont. Shelf Res.,* **34,** 30–40, doi:10.1016/j.csr.2011.11.017.

Kerry, C. G., B. S. Powell, and G. S. Carter, 2014: The impact of subtidal circulation on internal tide generation and propagation in the Philippine Sea. *J. Phys. Oceanogr.,* **44,** 1386–1405, doi:10.1175/JPO-D-13-0142.1.

Kersale, M., A. M. Doglioli, and A. A. Petrenko, 2011: Sensitivity study of the generation of mesoscale eddies in a numerical model of Hawaii Islands. *Ocean Sci.,* **7,** 277–291, doi:10.5194/os-7-277-2011.

Lewis, J. K., I. Shulman, and A. F. Blumberg, 1998: Assimilation of CODAR observations into ocean models. *Cont. Shelf Res.,* **18,** 541–559, doi:10.1016/S0278-4343(98)00006-5.

Lumpkin, C., 1998: Eddies and currents of the Hawaiian Islands. Ph.D. dissertation, University of Hawai'i at Mānoa, 282 pp.

Lumpkin, R., and P. Flament, 2001: Lagrangian statistics in the central North Pacific. *J. Mar. Syst.,* **29,** 141–155, doi:10.1016/S0924-7963(01)00014-8.

——, and ——, 2013: Extent and energetics of the Hawaiian Lee Countercurrent. *Oceanography,* **26,** 58–65, doi:10.5670/oceanog.2013.05.

Matthews, D., B. S. Powell, and I. Janeković, 2012: Analysis of four-dimensional variational state estimation of the Hawaiian waters. *J. Geophys. Res.,* **117,** C03013, doi:10.1029/2011JC007575.

Mellor, G. L., and T. Yamada, 1982: Development of a turbulence closure model for geophysical fluid problems. *Rev. Geophys. Space Phys.,* **20,** 851–875, doi:10.1029/RG020i004p00851.

Molemaker, M. J., J. C. McWilliams, and I. Yavneh, 2005: Baroclinic instability and loss of balance. *J. Phys. Oceanogr.,* **35,** 1505–1517, doi:10.1175/JPO2770.1.

——, ——, and X. Capet, 2010: Balanced and unbalanced routes to dissipation in an equilibrated Eady flow. *J. Fluid Mech.,* **654,** 35–63, doi:10.1017/S0022112009993272.

Murray, C. P., S. L. Morey, and J. O'Brien, 2001: Interannual variability of upper ocean vorticity balances in the Gulf of Alaska. *J. Geophys. Res.,* **106,** 4479–4491, doi:10.1029/1999JC000071.

Oka, E., and K. Ando, 2004: Stability of temperature and conductivity sensors of Argo profiling floats. *J. Oceanogr.,* **60,** 253–258, doi:10.1023/B:JOCE.0000038331.10108.79.

Powell, B. S., H. Arango, A. Moore, E. Di Lorenzo, R. Milliff, and D. Foley, 2008: 4DVAR data assimilation in the Intra-Americas Sea with the Regional Ocean Modeling System (ROMS). *Ocean Modell.,* **23,** 130–145, doi:10.1016/j.ocemod.2008.04.008.

——, I. Janeković, G. S. Carter, and M. A. Merrifield, 2012: Sensitivity of internal tide generation in Hawaii. *Geophys. Res. Lett.,* **39,** L10606, doi:10.1029/2012GL051724.

Qiu, B., D. A. Koh, C. Lumpkin, and P. Flament, 1997: Existence and formation mechanism of the North Hawaiian Ridge Current. *J. Phys. Oceanogr.,* **27,** 431–444, doi:10.1175/1520-0485(1997)027<0431:EAFMOT>2.0.CO;2.

Qu, T., J. Gan, A. Ishida, Y. Kashino, and T. Tozuka, 2008: Semiannual variation in the western tropical Pacific Ocean. *Geophys. Res. Lett.,* **35,** L16602, doi:10.1029/2008GL035058.

Ray, R. D., and G. T. Mitchum, 1996: Surface manifestation of internal tides generated near Hawaii. *Geophys. Res. Lett.,* **23,** 2101–2104, doi:10.1029/96GL02050.

——, and ——, 1997: Surface manifestation of internal tides in the deep ocean: Observations from altimetry and island gauges. *Prog. Oceanogr.,* **40,** 135–162, doi:10.1016/S0079-6611(97)00025-6.

Sasaki, H., and P. Klein, 2012: SSH wavenumber spectra in the North Pacific from a high-resolution realistic simulation. *J. Phys. Oceanogr.,* **42,** 1233–1241, doi:10.1175/JPO-D-11-0180.1.

——, B. Taguchi, N. Komori, and Y. Masumoto, 2013: Influence of local dynamical air–sea feedback process on the Hawaiian Lee Countercurrent. *J. Climate,* **26,** 7267–7279, doi:10.1175/JCLI-D-12-00586.1.

Schwab, D. J., and D. Beletsky, 2003: Relative effects of wind stress curl, topography, and stratification on large-scale circulation in Lake Michigan. *J. Geophys. Res.,* **108,** 3044, doi:10.1029/2001JC001066.

Shchepetkin, A. F., and J. C. McWilliams, 2005: The Regional Oceanic Modeling System (ROMS): A split-explicit, free-surface, topography-following-coordinate oceanic model. *Ocean Modell.,* **9,** 347–404, doi:10.1016/j.ocemod.2004.08.002.

——, and ——, 2009: Correction and commentary for ''Ocean forecasting in terrain-following coordinates: Formulation and skill assessment of the regional ocean modeling system'' by Haidvogel et al., J. Comp. Phys. 227, pp. 3595–3624. *J. Comput. Phys.,* **228,** 8985–9000, doi:10.1016/j.jcp.2009.09.002.

Shulman, I., and J. D. Paduan, 2009: Assimilation of HF radar-derived radials and total currents in the Monterey Bay area. *Deep-Sea Res. II,* **56,** 149–160, doi:10.1016/j.dsr2.2008.08.004.

Smith, K. S., and G. K. Vallis, 2001: The scales and equilibration of midocean eddies: Freely evolving flow. *J. Phys. Oceanogr.,* **31,** 554–571, doi:10.1175/1520-0485(2001)031<0554:TSAEOM>2.0.CO;2.

Thomas, L. N., 2005: Destruction of potential vorticity by winds. *J. Phys. Oceanogr.,* **35,** 2457–2466, doi:10.1175/JPO2830.1.

Tu, C. C., and Y. L. Chen, 2011: Favorable conditions for the development of a heavy rainfall event over Oahu during the 2006 wet period. *Wea. Forecasting,* **26,** 280–300, doi:10.1175/2010WAF2222449.1.

Waite, M., and P. Bartello, 2006: The transition from geostrophic to stratified turbulence. *J. Fluid Mech.,* **568,** 89–108, doi:10.1017/S0022112006002060.

Xie, S. P., W. T. Liu, Q. Liu, and M. Nonaka, 2001: Far-reaching effects of the Hawaiian Islands on the Pacific Ocean-atmosphere system. *Science,* **292,** 2057–2060, doi:10.1126/science.1059781.

Xu, Y., and L. L. Fu, 2011: Global variability of the wavenumber spectrum of oceanic mesoscale turbulence. *J. Phys. Oceanogr.,* **41,** 802–809, doi:10.1175/2010JPO4558.1.

Zilberman, N. V., M. M. Merrifield, G. S. Carter, D. S. Luther, M. D. Levine, and T. J. Boyd, 2011: Incoherent nature of M_2 internal tides at the Hawaiian Ridge. *J. Phys. Oceanogr.,* **41,** 2021–2036, doi:10.1175/JPO-D-10-05009.1.